Geophysical Research Letters

RESEARCH LETTER
10.1029/2025GL120067

Evidence for Virtual Source-Receiver Refractions in Cross Correlations of Infrasonic Ambient Noise

L. G. Evers[1,2], J. D. Assink[1], and J. T. Fricke[3]

[1]R&D Department of Seismology and Acoustics, Royal Netherlands Meteorological Institute (KNMI), De Bilt, The Netherlands, [2]Department of Geoscience and Engineering, Faculty of Civil Engineering and Geosciences, Delft University of Technology, Delft, The Netherlands, [3]DGMR, The Hague, The Netherlands

Key Points:

- The cross correlation of infrasonic ambient revealed coherent energy from microbaroms and surf from a broad-band analysis
- Seasonal variability was retrieved in source and medium variations in 11 years of microbarometer data
- Stratospheric virtual source-receiver refractions can explain the unusual short lag times, providing new means to probe the upper atmosphere

Correspondence to:
L. G. Evers,
evers@knmi.nl

Citation:
Evers, L. G., Assink, J. D., & Fricke, J. T. (2026). Evidence for virtual source-receiver refractions in cross correlations of infrasonic ambient noise. *Geophysical Research Letters*, *53*, e2025GL120067. https://doi.org/10.1029/2025GL120067

Received 16 OCT 2025
Accepted 3 JAN 2026

Abstract Seasonal variability in source activity and atmospheric temperature were retrieved from 11 years of infrasonic ambient noise. Variable lag times between an array and single microbarometer were obtained from envelopes of cross-correlation functions. Beamforming and one-bit normalization significantly enhanced the stationary phase. Both microbaroms and surf appeared abundantly present, in the 0.1–2.0 Hz frequency band. Modeling revealed both tropospheric and stratospheric propagation of the infrasound, following traditional and more unconventional propagation mechanisms. Virtual source-receiver refractions from stratospheric altitudes appeared a plausible explanation for the unusual short lag times, which allows for new ways to passively probe the stratosphere.

Plain Language Summary Microbarometers measure infrasound from the background noise field, that is, ambient noise. This ambient noise is continuously present and generated by oceanic waves. The sound speed is a function of wind and temperature and determines how fast the ambient noise travels from one to another microbarometer. The so-called travel time can be obtained by comparing the recordings of ambient noise of different microbarometers. The use of advanced processing techniques with multiple microbarometers was explored and enhanced the results. The observed travel times provided evidence for propagation through the upper atmosphere, that is, the stratosphere. New ways are proposed to apply surface-based infrasound recordings in passively probing stratospheric wind and temperature conditions.

1. Introduction

Haney (2009) was the first to show the application of interferometry to infrasonic ambient noise to 18 days of recordings at two infrasonic microphones over a range of 13.5 km. Haney (2009) focused on the microbarom peak, around 0.2 Hz, resulting from oceanic wave-wave interaction (Posmentier, 1967; Waxler & Gilbert, 2006). The theoretical foundation for Green's function retrieval in a moving medium was earlier and simultaneously provided by Godin (2006) and Wapenaar (2006). Building upon this work, Fricke et al. (2014) further used interferometry in analyzing the influence of the troposphere on infrasonic propagation and wavefront coherency from array observations. Fricke (2016) showed promising results in infrasonic interferometry applied to microbarometers in Alaska (US). The cross-correlation functions (CCFs) of microbarometer pairs appeared sensitive to tropospheric wind and temperature. More recently, Ortiz et al. (2022) showed the application of auto-correlation infrasonic interferometry on Mars in retrieving changes in atmospheric wind and temperature.

The current study extends earlier research by applying cross correlations to long-time series, by using a micro-barometer array and single microbarometer and by enlarging the frequency range.

Figure 1 shows the I53US microbarometer array and a single microbarometer at Poker Flat Research Range (POKR) in Alaska. I53US is part of the International Monitoring System, in place for the verification of the Comprehensive Nuclear-Test-Ban Treaty (Dahlman et al., 2009). I53US consists of eight microbarometers forming an array with an aperture of approximately 2 km. Data is provided to Earthscope since 2002-06-24. POKR has been operational since 2012-10-02, first as part of the USArray Transportable Array (TA), later it was included in the Alaska Geophysical Network (AK). The distance between the two is 34.34 km, while the azimuths connecting the center of the array and POKR are 35.50° (pointing to the northeast) and 215.88° (to the southwest). This set up allows for the use of array beams rather than cross correlating single microbarometers. The advantage of using array beams over single stations has been shown by, for example, Ruigrok et al. (2017) in seismological and Evers et al. (2017) in hydro-acoustical cross correlation calculations. In essence, beamforming increases the

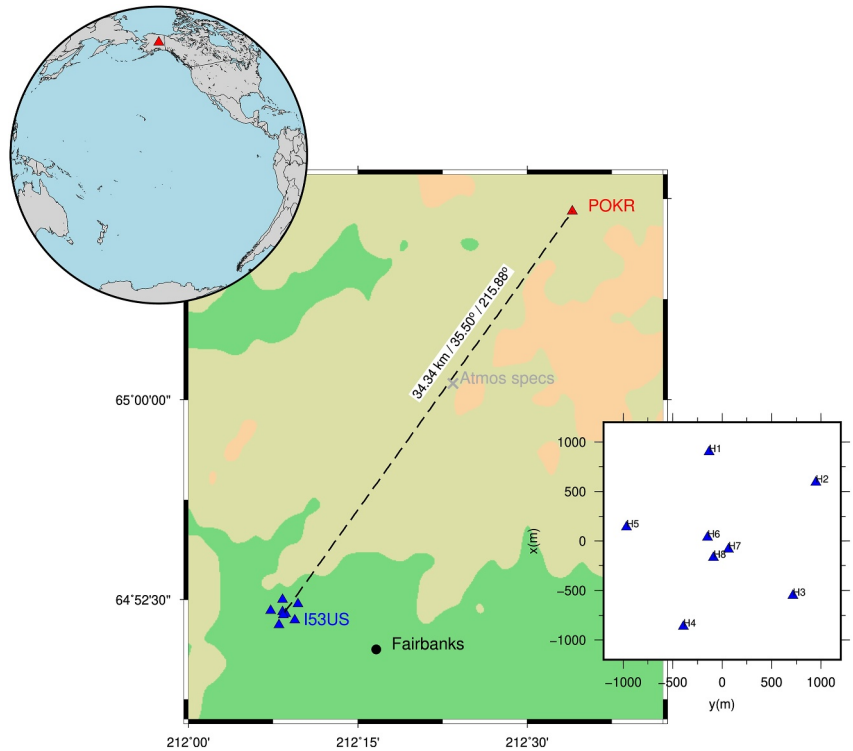

Figure 1. IMS array I53US and infrasonic station POKR in Alaska, US. I53US consists of eight microbarometers (H1..H8) in an array with an aperture of ∼2 km; POKR consists of one microbarometer. I53US has been providing data to Earthscope since 2002-06-24 and POKR since 2012-10-02. POKR started of as part of the USArray Transportable Array (network: TA) and was continued on 2020-02-12 as part of the Alaska Geophysical Network (AK). The center of the array is at a distance of 34.34 km from POKR, at azimuths of 35.50° and 215.88°. The gray cross indicates the location [147.61°W, 65.01°N] for which ERA5 atmospheric specifications were acquired.

signal-to-noise ratio (SNR) through signal summation and focuses on the stationary phase along the mentioned endfire azimuths (Wapenaar, 2006).

Most earlier work used microbaroms in interferometry, typically by applying band-pass filters between 0.1 and 0.3 up to 0.5 Hz. Here, this frequency range is extended to 2.0 Hz, to include surf which is abundantly present in the ambient noise field (M. Garcés et al., 2003). Breaking oceanic waves on the coast line lead to infrasound from surf, usually observed in coastal areas and on oceanic islands (Francoeur et al., 2025; Le Pichon et al., 2004; Lyons et al., 2014).

This letter is organized as follows: Section 2 describes various approaches to calculating CCFs from pairs of microbarometers and with array beams. Envelopes of the CCFs are calculated to pick the lag times at maximum correlation. Propagation modeling is added in Section 3 to analyze which atmospheric conditions allowed energy to travel from I53US in POKR. Furthermore, various propagation mechanisms will be analyzed, such as: tropospheric refractions, direct waves, partial reflections and virtual source-receiver refractions. These results are discussed in Section 4 in terms of ambient noise, atmospheric variability and infrasonic propagation. Finally, conclusions are drawn in Section 5 describing the advantage of using long-time series, array beams, extended frequency bands and virtual source-receiver refractions also in future applications.

2. Lag Times Between I53US and POKR

2.1. Cross-Correlation Functions (CCFs)

Based on the data availability at Earthscope, 11 years of microbarometer data from I53US and POKR was acquired. The data was bandpass filtered with a second order Butterworth filter having corner frequencies of 0.1 and 2.0 Hz. Cross-correlations functions (CCFs) were calculated per day from 2014 up to 2024. Figure 2 shows the

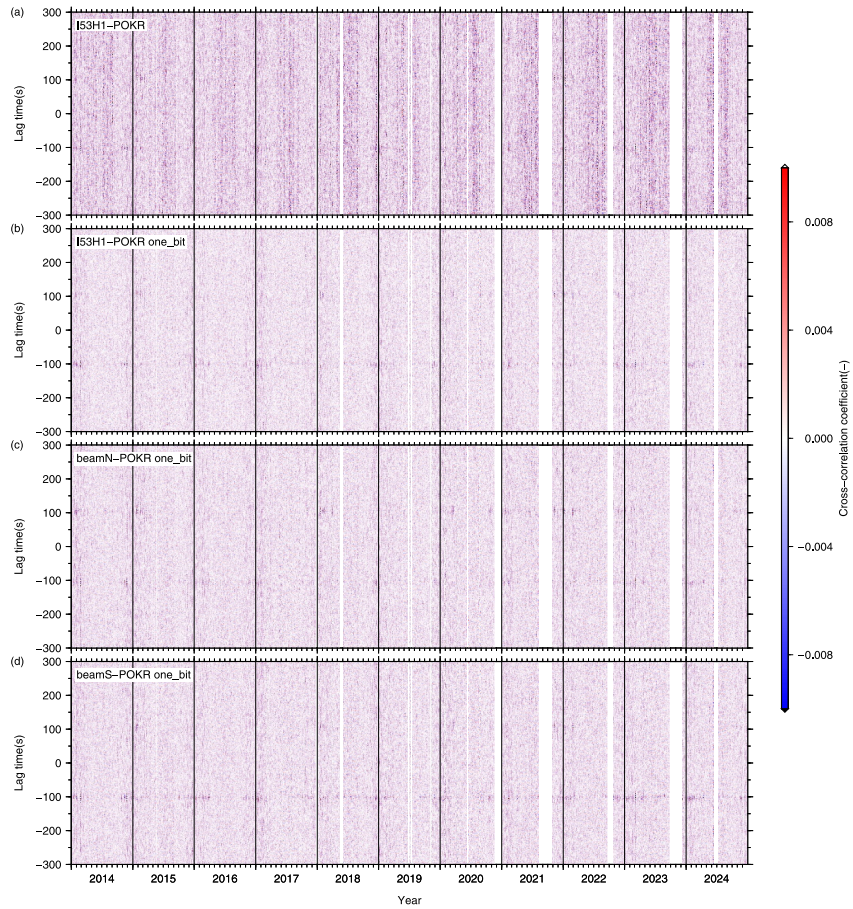

Figure 2. Cross-correlation functions (CCFs) per day for microbarometer pair I53H1 and POKR and array beams and POKR. The data were bandpass filtered between 0.1 and 2.0 Hz. Shown are: (a) daily CCFs for I53H1 and POKR, (b) I53H1 and POKR with one bit normalization, (c) the beam of I53US toward the North (beamN) and POKR one bit normalized and (d) the beam toward the South (beamS) and POKR one bit normalized. BeamN and beamS were formed with a beam velocity of 340 m/s and azimuth of 35.50° and 215.88°, respectively. Days for which no data could be obtained from Earthscope, for either I53US or POKR or both, are left blank.

results for both microbarometer pairs (I53H1 and POKR) and array beams with POKR. The configuration was chosen such that positive lag times corresponded to propagation from POKR to I53US and negative times vice verse. The CCFs for I53H1-POKR show hardly any energy in the stationary phase (Figure 2a). Upon close inspection, some coherent energy can be found for example, around −100s early 2017 and +100s late 2021.

To suppress the contribution of transient signals, one-bit normalization was applied to the data prior to calculating the CCFs (Bensen et al., 2007). This clearly had its effect as can be seen in Figure 2b. Coherent energy from both a northerly and southerly direction started to show up throughout the years. Energy coming from the south, that is, at negative lag times, seemed more dominantly present than energy from the north. It thus appeared that both the causal and acausal part of the CCFs are stationarily resolved.

To further enhance the CCFs, beamforming was applied to the I53US array. One beam was formed towards the northerly endfire at an azimuth of 35.50° and one in a southerly direction at 215.88°. The slowness for beamforming consists both of an azimuth and a beam velocity. For the latter 340 m/s was chosen, furthermore, bandpass filtering and one-bit normalization were again applied. Figure 2c shows the results for the northerly beam (beamN) and Figure 2d for beam towards the South (beamS).

Compared to the pairwise microbarometer CCFs, the beams further increased the SNR of the stationary phase. BeamS intensified the energy coming from a southerly direction, while beamN did so for energy arriving from the North. As noted earlier, the acausal part appeared stronger than the causal part. This can also be seen in Figure 2c,

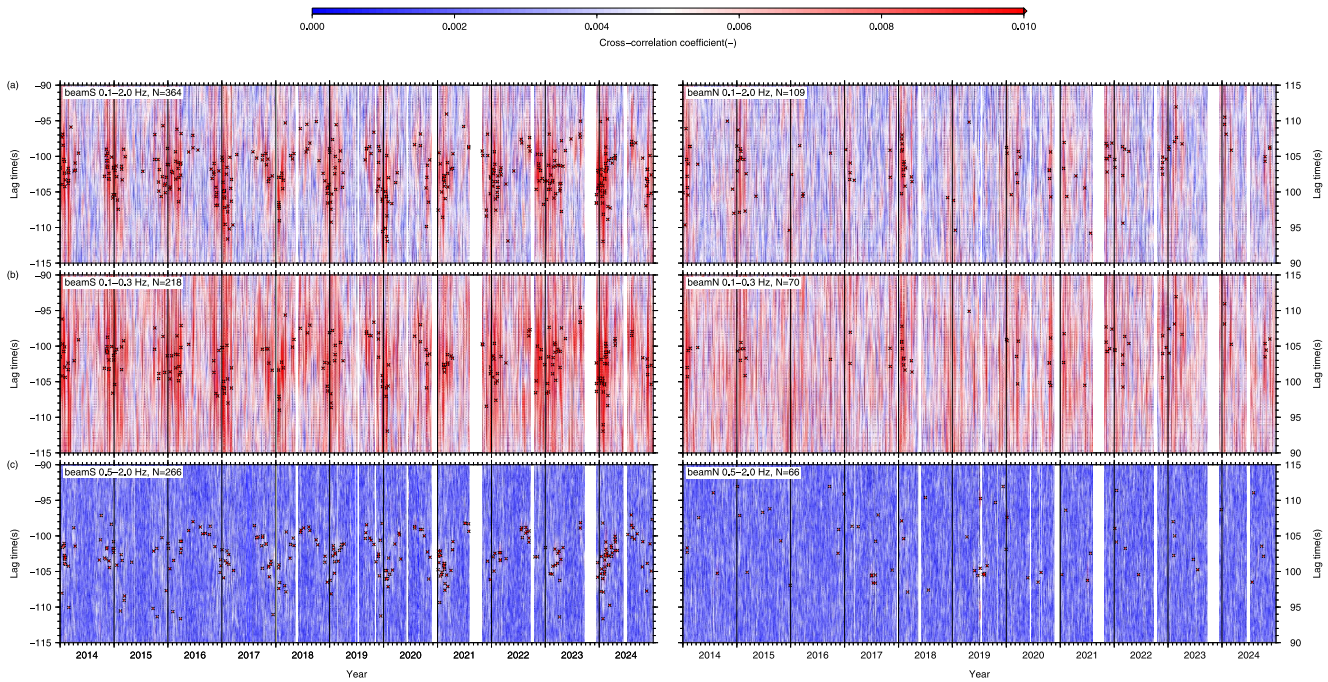

Figure 3. Envelopes of the daily cross-correlation functions (CCFs) from beamS (left) and beamN (right) with POKR. One-bit normalization was applied prior to cross correlating the data. Different frequency bands are shown, following from the applied Butterworth bandpass filter: row (a) 0.1–2.0 Hz, (b) 0.1–0.3 Hz and (c) 0.5–2.0 Hz. The dots (color coded according to the color bar) and corresponding crosses indicate the maxima of daily CCF envelopes above a certain threshold, which was set to: 0.015 (0.1–2.0 Hz), 0.02 (0.1–0.3 Hz) and 0.008 (0.5–2.0 Hz). The resulting number of detections (N) are given in the label within each frame.

where energy from the South was still leaking through while focusing on the North. This was less the case for beamS (Figure 2d), where energy from the northerly endfire hardly showed up.

In the next section, these results will be further refined by extracting the maxima of the CCFs and associated lag times.

2.2. CCF Envelopes

In the analyzed frequency range, both infrasound from microbaroms and surf are present. Envelopes of the one-bit normalized CCFs were calculated to better interpret the results and to pick the maxima and corresponding lag times. Figure 3 shows the envelopes in the different frequency bands for both beamS and beamN cross correlated with POKR. The full band runs from 0.1 to 2.0 Hz (Figure 3a), the microbarom band from 0.1 to 0.3 Hz (Figure 3b) and the surf frequency band from 0.5 to 2.0 Hz (Figure 3c). The maxima of the envelopes were automatically picked by setting a certain threshold which was found by trial and error. A too high threshold would lead to few detected maxima, a too low one to many unreasonably large or small lag times. The following thresholds were chosen: 0.015 (0.1–2.0 Hz), 0.02 (0.1–0.3 Hz) and 0.008 (0.5–2.0 Hz). The resulting maxima are indicated in Figure 3, also the number of detected maxima (N) is given. As expected, most detections were made in the acausal part. The acausal part had about three times more detections than the causal part, within the full and microbarom band. The surf band had significantly fewer detections in the causal part, that is, about four times less. The maxima seemed to follow a seasonal pattern of large lag times in winter and smaller values in summer. This will be further addressed in the next section by adding propagation modeling to the analysis. For this the largest number of detections ($N = 364$) will be used, that are those from the acausal part in the full band from the beamS CCFs.

The number of detections for the beams, in the different bands and acausal and causal part will be further discussed in Section 4, after the propagation modeling will be added to the analysis in the next section.

3. Infrasonic Propagation

The propagation of infrasound is dependent on the temperature and wind in the atmosphere. The effective sound speed (c_{eff}) consists of the temperature effect and projects the wind in the source-receiver direction. The atmospheric specifications of temperature and wind were obtained from ERA5, the fifth generation ECMWF atmospheric reanalysis, for [147.61°W, 65.01°N], which is halfway between I53US and POKR (see Figure 1), at 00 hr UTC. ECMWF stands for the European Centre for Medium-Range Weather Forecasts. In this section, various propagation mechanisms will be considered to model the observed lag times.

Propagation was considered between I53US and POKR, where I53US acted as a source for POKR. Such a configuration was allowed for since the stationary phase was resolved, both causally and acausally (Wapenaar, 2006).

First, tropospheric refractions were considered (Figure 4a), by applying geometrical raytracing through the 1D atmospheric models (M. A. Garcés et al., 1998). Tropospheric refractions occurred due to a positive gradient in the c_{eff}, bending the upward traveling rays back to the receiver. A temperature inversion possibly combined with an increase in the wind with altitude could provide such propagation conditions. The modeled lag times are shown in Figure 4b, where for 280 out of the 364 detections favorable atmospheric conditions existed.

Second, direct propagation between the source and receiver was considered, to explain all 364 detections. Such guided waves were also considered by Haney (2009) and were expected to exist for short source-receiver distances. For this type of propagation, the average c_{eff} in the first 3 km of atmosphere was calculated. The resulting lag times are shown in Figure 4b.

Third, partial reflections in the troposphere were considered (Kulichkov et al., 2010). Small scale structure in the atmosphere may lead to partial reflections (Figure 4a). Such variations are caused by gravity waves and are not resolved in the atmospheric models, as used here (Chunchuzov et al., 2015). Figure 4c shows examples of the lag times assuming partial reflections to have taken place at 3.5 and 5 km altitude.

Fourthly, virtual source-receiver refractions in the troposphere and stratosphere were considered, because the various traditional tropospheric propagation paths can not explain the observed shorter lag times, hence the need for a higher c_{eff}. Virtual source-receiver refractions have been observed in seismological CCFs calculations as spurious and also useful arrivals (Mikesell et al., 2009; Ruigrok et al., 2012). An example is shown in Figure 4a, where the lag time is determined by the maximum c_{eff} at a certain altitude. The corresponding lag times are shown in Figure 4d, which were calculated based on the $c_{eff,max}$ in the troposphere or stratosphere.

In addition, Figures 4b–4d shows the temperature at the earth's surface from ERA5 specifications, to illustrate the correspondence between lag time and temperature as a function of the time of year. No agreement between the absolutes values of surface temperature and lag time is expected.

In the next section, these modeling results will be discussed also taking into account the seasonal variations in source activity and atmospheric conditions.

4. Discussion

1. On the ambient noise: microbaroms are generated in the Atlantic (to the North) and Pacific Ocean (South) (Den Ouden et al., 2020; Smets & Evers, 2014). During the northern hemisphere winter, microbaroms are strongest due to storm activity increasing the oceanic wave-wave interaction (Matoza et al., 2013). Microseism, the microbarom equivalent in the solid earth, show a similar seasonal dependence in strength (Pandey et al., 2025). This seasonal effect can clearly be seen in the CCFs and their envelopes. The acausal part is stronger because the source of Pacific microbaroms is closer to I53US-POKR than the Atlantic source. Microbaroms also appear during winter on beamN.
   Microbaroms can be expected from the Arctic Ocean in summer, as microseism have also been observed (Chen et al., 2025). However, on beamN no such activity was found.
   Surf can come from the Pacific coast line (South) and the northern coast line with the Beaufort Sea. Detections are made throughout the year on beamS, with most detections in winter when near-coastal oceanic wave activity is the highest. Hardly any surf detections are made on beamN, as the Beaufort Sea is mostly frozen. Some detections occur is summer, for example, in 2017 and 2019.

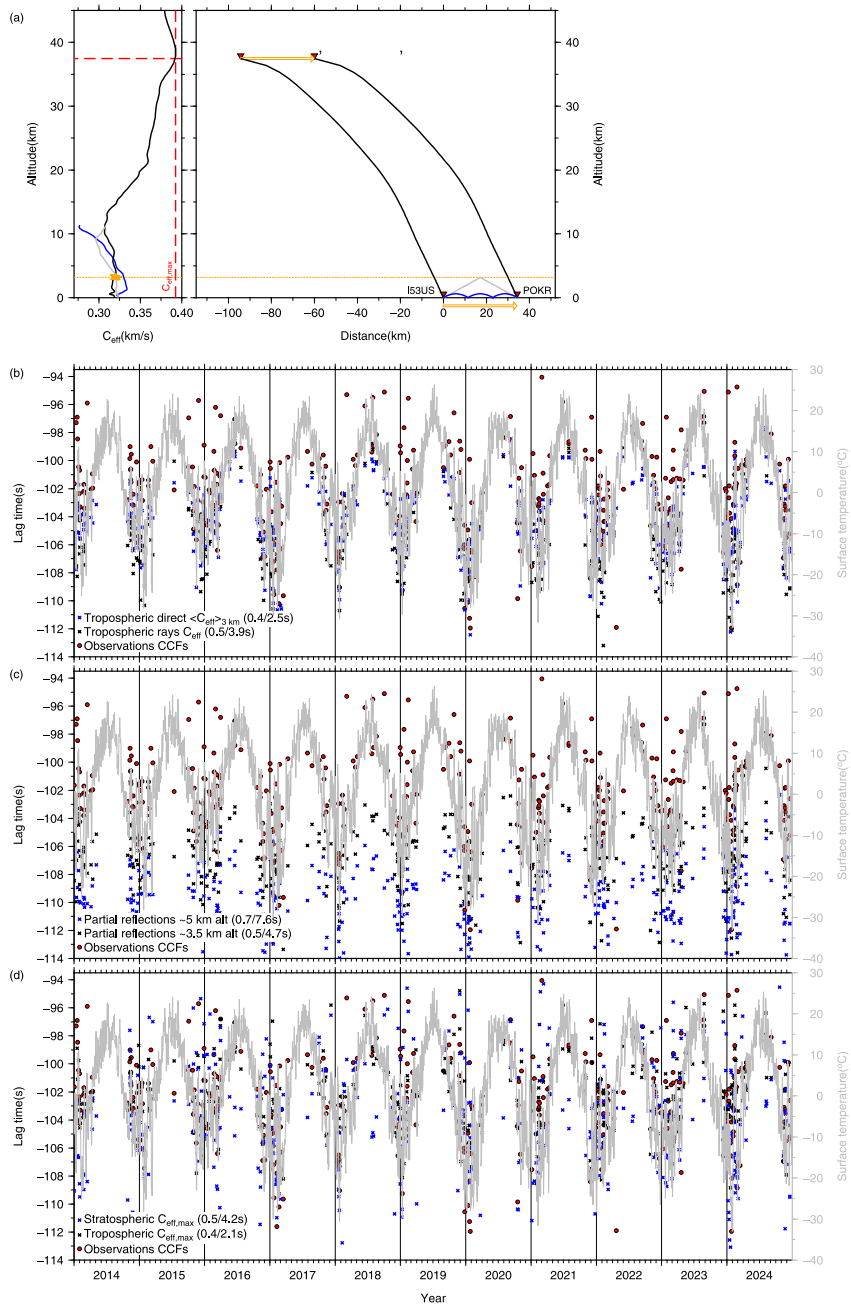

Figure 4. Modeled lag times for various propagation mechanisms between I53US (source) and POKR (receiver), denoted by the red triangles. (a) Effective sound speed profiles (left) and propagation paths (right) for tropospheric refractions (blue), partial reflections (gray) and virtual source-receiver refractions (black). Partial reflections are caused by small scale structure as cartooned in orange. Virtual source-receiver refractions are illustrated by a virtual source and receiver at altitude (red triangles with apostrophe), where propagation is determined by $c_{eff,max}$ between the two (orange vector). (b) Modeled lag times for tropospheric refractions from raytracing (black crosses) and direct propagation with $<c_{eff}>_{3km}$ (blue). (c) Examples of modeled lag times for partial reflections from 3.5 km (black) and 5 km (blue) altitude. (d) Lag times for virtual source-receiver refractions based on $c_{eff,max}$ in the troposphere (black) and stratosphere (blue). The Root Mean Square (RMS) residuals and Mean Absolute Errors (MAE) in seconds are given between brackets in each label (RMS/MAE), following: RMS $= \sqrt{\left(\frac{\sum_{i=1}^{N}(t_{i,model}-t_{i,obs})^2}{N}\right)}$ and MAE $= \frac{\sum_{i=1}^{N}|t_{i,model}-t_{i,obs}|}{N}$. The observed lag times from the CCF envelopes for beamS (0.1–2.0 Hz) are given as red dots in frames b-d, the surface temperature is given in gray. The latter is given to illustrate the seasonalityin the lag times, no agreement between the absolute values of temperature and lag times is expected.

2. On the processing: bandpass filtering, one-bit normalization and beamforming significantly enhances the results by focusing on stationary phase. Most detections on the CCF envelopes are made on the broad-band results (0.1–2.0 Hz). Increasing the beam velocity of 340 m/s to 400 m/s, to allow for possible steeper incidence angles, did not significantly change the results. However, this might still be a worthwhile approach when cross correlating the beams of two arrays.
   Stacking of CCFs is often applied in seismic (Bensen et al., 2007) or hydro-acoustical applications (Evers, 2025; Woolfe et al., 2015). However, the daily variations in the atmosphere are such that the lag times vary by seconds. Time averaged stacks will cancel out the coherent energy, rather than constructively adding to the stationary phase. It was found that daily cross correlations give the best results, without further stacking. Too few energy was present in hourly CCFs, even when selecting hours with high microbarom or surf activity.
3. On the atmospheric temperature: the lag times appeared to follow a seasonal trend of low values in summer and high values in winter. Such a trend corresponds to the seasonal variations atmospheric temperature, as it strongly determines the c_{eff}. In summer, higher temperatures lead to a higher c_{eff} and hence smaller lag times and vice verse in winter. Variations around this background trend will be addressed in the next item.
4. On the propagation modeling: conventional propagation could only partly explain the observations. Lag times up to about −98s were modeled with traditional tropospheric refractions, direct waves and low-level partial reflections. I53US acted as a source for POKR following the interferometric approach to ambient noise resolving the stationary phase. However, the observed smaller lag times needed an unconventional approach by introducing virtual source-receiver refractions to model the observed smaller lag times from $c_{eff,max}$ in the tropo- and stratosphere. The stratospheric wave guide is far more stable than the tropospheric duct, in long range infrasound propagation (Le Pichon et al., 2012). The observed reciprocity also requires a stable laminar flow, in order to interchange source and receiver positions (Godin, 2006; Wapenaar, 2006). The flow in the troposphere is turbulent (Smink et al., 2019) and the lateral variations are strong (Blom et al., 2023). Therefore, the qualitative evidence for stratospheric virtual source-receiver refractions is stronger than for those from tropospheric altitudes.

The Root Mean Square (RMS) residuals and Mean Absolute Errors (MAE) are given in each label within each frame of Figure 4. These misfits are merely given to aid in visually interpreting the results. The lag times follow from daily (24 hr) cross correlations, while the atmospheric specifications are valid for 00 hr UTC. Therefore, over-interpreting misfits of the order of tenths to a few seconds should be avoided.

Following the above discussion, conclusions will be drawn in the next section and venues for future research will be explored, based on the application of infrasonic virtual source-receiver refractions.

5. Conclusions

Both the causal and acausal part of the CCFs were consistently resolved from infrasonic ambient noise. For this, 11 years of microbarometer data was used from an array (I53US) and single microbarometer (POKR) in Alaska, with an inter-station distance of 34.34 km. With respect to earlier studies, the frequency range was extended from 0.1 to 2.0 Hz, to include both infrasound from microbaroms and surf. Furthermore, beamforming and one-bit normalization was applied to significantly enhance the stationary phase. Lag times were retrieved from CCF envelopes.

Raytracing through actual atmospheric specifications (ERA5) could partly explain the obtained lag times, with conventional tropospheric refractions, direct waves and possibly partial reflections. Evidence for stratospheric virtual source-receiver refractions was found in order to explain the unusual small lag times. The latter need a high c_{eff}, which was unlikely to be provided by conventional tropospheric propagation.

Seasonal variations in atmospheric temperature explained the general trend of small lag times in summer and large values in winter.

The extended frequency range will also better constrain the inversion of dispersion curves for group velocity and hence the retrieval of atmospheric wind and temperature, based on a broad-band analysis (Haney, 2009).

Up to now, it was thought that the stratospheric stationary phase could only be resolved with a source-receiver distance of at least 200 km, which allows for a stratospheric refraction to be observed (Arrowsmith et al., 2016; Fricke et al., 2013). The stratospheric stationary phase has not been found till now, due to the lack of

signal coherency. Virtual source-receiver stratospheric refractions strongly reduce this distance. In essence, a virtual source and receiver can be placed at altitude with the same inter-station distance as the true receivers. Detailed knowledge on the source characteristics and propagation from the far field become irrelevant, since the stationary phase from the microbarom and surf region was resolved. The c_{eff} at altitude can directly be measured with surface-based receivers, from the phase differences between the virtual source-receiver pair. With this, the application of infrasound as a passive probe for stratospheric wind and temperature becomes far more feasible. Signal coherency is higher at shorter distances, as the SNR is less affected by the turbulent troposphere.

In conclusion, the here proposed processing techniques and evidence for virtual source-receiver refractions allow for new ways to image the (upper) atmosphere.

Conflict of Interest

The authors declare no conflicts of interest relevant to this study.

Data Availability Statement

The infrasonic data from I53US and POKR were obtained from the Earthscope Consortium, by using their International Federation of Digital Seismograph Networks (FDSN) webservices at https://service.iris.edu/fdsnws/dataselect/1/.

POKR is part of the Alaska Geophysical Network (Alaska Earthquake Center, Univ. of Alaska Fairbanks, 1987).

The ERA5 atmospheric specifications for temperature and wind used in this study were obtained from the Climate Data Store (Muñoz Sabater, 2019).

CCFs and their envelopes were calculated with the Seismic Analysis Code software, which is available from the EarthScope Consortium (https://ds.iris.edu/ds/nodes/dmc/forms/sac/).

Acknowledgments
The authors thank the CTBTO and its station operators for providing high-quality and continuous IMS recordings. The colleagues responsible for the Alaska Geophysical Network are thanked for providing the excellent microbarometer data used in this study. Drs E. Ruigrok and C. Weemstra (KNMI) are thanked for fruitful discussions on data processing, interpretation and on virtual refractions in seismological CCFs. Drs M. Haney (USGS/AVO) and R. Waxler (OleMiss/NCPA) are thanked for their constructive reviews of this letter, which helped in improving the manuscript. Figures in this letter were made with the Generic Mapping Tools (Wessel et al., 2013).

References

Alaska Earthquake Center, Univ. of Alaska Fairbanks. (1987). Alaska geophysical network. *International Federation of Digital Seismograph Networks*. https://doi.org/10.7914/SN/AK

Arrowsmith, M., S. Arrowsmith, S., & Marcillo, O. (2016). Using sounds from the ocean to measure winds in the stratosphere. *Eos, Transactions American Geophysical Union*, *97*. https://doi.org/10.1029/2016eo042563

Bensen, G. D., Ritzwoller, M. H., Barmin, M. P., Levshin, A. L., Lin, F., Moschetti, M. P., et al. (2007). Processing seismic ambient noise data to obtain reliable broad-band surface wave dispersion measurements. *Geophysical Journal International*, *169*(3), 1239–1260. https://doi.org/10.1111/j.1365-246x.2007.03374.x

Blom, P., Waxler, R., & Frazier, G. (2023). Quantification of spatial and seasonal trends in the atmosphere and construction of statistical models for infrasonic propagation. *Geophysical Journal International*, *235*(2), 1007–1020. https://doi.org/10.1093/gji/ggad260

Chen, J.-C. F., Park, S., & MacAyeal, D. R. (2025). Tracking multiyear sea-ice variation in the Arctic Ocean over decades with microseism. *Geophysical Research Letters*, *52*(2), e2024GL111159. https://doi.org/10.1029/2024gl111159

Chunchuzov, I., Kulichkov, S., Popov, O., Perepelkin, V., Vasil'ev, A., Glushkov, A., & Firstov, P. (2015). Characteristics of a fine vertical wind field structure in the stratosphere and lower thermosphere according to infrasonic signals in the zone of acoustic shadow. *Izvestiya - Atmospheric and Oceanic Physics*, *51*(1), 57–74. https://doi.org/10.1134/s0001433814060061

Dahlman, O., Mykkeltveit, P., & Haak, H. (2009). Monitoring technologies. In *Nuclear Test Ban* (pp. 1–34). Springer.

Den Ouden, O. F. C., Assink, J. D., Smets, P. S. M., Shani-Kadmiel, S., Averbuch, G., & Evers, L. G. (2020). CLEAN beamforming for the enhanced detection of multiple infrasonic sources. *Geophysical Journal International*, *221*(1), 305–317. https://doi.org/10.1093/gji/ggaa010

Evers, L. G. (2025). Decadal observations of deep ocean temperature change passively probed with acoustic waves. *JASA Express Letters*, *5*(7), 076001. https://doi.org/10.1121/10.0037200

Evers, L. G., Wapenaar, K., Heaney, K. D., & Snellen, M. (2017). Deep ocean sound speed characteristics passively derived from the ambient acoustic noise field. *Geophysical Journal International*, *210*(1), 27–33. https://doi.org/10.1093/gji/ggx061

Francoeur, J. W., Matoza, R. S., Ortiz, H. D., & De Negri, R. (2025). Identification of transient seismo-acoustic signals from crashing ocean waves: Template matching and location of discrete surf events. *Geophysical Journal International*, ggaf317. https://doi.org/10.1093/gji/ggaf317

Fricke, J. T. (2016). *Infrasonic interferometry: Probing the atmosphere with acoustic noise from the oceans (unpublished doctoral dissertation)*. Delft University of Technology. Retrieved from http://resolver.tudelft.nl/uuid:6d23ede7-8f1f-494e-930c-e2ecc6546160

Fricke, J. T., Allouche, N. E., Simons, D. G., Ruigrok, E. N., Wapenaar, K., & Evers, L. G. (2013). Infrasonic interferometry of stratospherically refracted microbaroms—A numerical study. *Journal of the Acoustical Society of America*, *134*(4), 2660–2668. https://doi.org/10.1121/1.4819117

Fricke, J. T., Evers, L. G., Smets, P. S. M., Wapenaar, K., & Simons, D. G. (2014). Infrasonic interferometry applied to microbaroms observed at the Large Aperture Infrasound Array in the Netherlands. *Journal of Geophysical Research*, *119*(16), 9654–9665. https://doi.org/10.1002/2014jd021663

Garcés, M., Hetzer, C., Merrifield, M., Willis, M., & Aucan, J. (2003). Observations of surf infrasound in Hawai'i. *Geophysical Research Letters*, *30*(24), 2264. https://doi.org/10.1029/2003GL018614

Garcés, M. A., Hansen, R. A., & Lindquist, K. G. (1998). Traveltimes for infrasonic waves propagating in a stratified atmosphere. *Geophysical Journal International*, *135*(1), 255–263. https://doi.org/10.1046/j.1365-246x.1998.00618.x

Godin, O. (2006). Recovering the acoustic Green's function from ambient noise cross correlation in an inhomogeneous moving medium. *Physical Review Letters*, *97*(5), 054301+. https://doi.org/10.1103/physrevlett.97.054301

Haney, M. M. (2009). Infrasonic ambient noise interferometry from correlations of microbaroms. *Geophysical Research Letters*, *36*(19), L19808. https://doi.org/10.1029/2009gl040179

Kulichkov, S. N., Chunchuzov, I. P., & Popov, O. I. (2010). Simulating the influence of an atmospheric fine inhomogeneous structure on long-range propagation of pulsed acoustic signals. *Izvestiya - Atmospheric and Oceanic Physics*, *46*(1), 60–68. https://doi.org/10.1134/s0001433810010093

Le Pichon, A., Ceranna, L., & Vergoz, J. (2012). Incorporating numerical modeling into estimates of the detection capability of the IMS infrasound network. *Journal of Geophysical Research*, *117*(D5), D05121. https://doi.org/10.1029/2011jd016670

Le Pichon, A., Maurer, V., Raymond, D., & Hyvernaud, O. (2004). Infrasound from ocean waves observed in Tahiti. *Geophysical Research Letters*, *31*(19), L19103. https://doi.org/10.1029/2004gl020676

Lyons, J. J., Haney, M. M., Fee, D., & Paskievitch, J. F. (2014). Distinguishing high surf from volcanic long-period earthquakes. *Geophysical Research Letters*, *41*(4), 1171–1178. https://doi.org/10.1002/2013gl058954

Matoza, R. S., Landès, M., Le Pichon, A., Ceranna, L., & Brown, D. (2013). Coherent ambient infrasound recorded by the International Monitoring System. *Geophysical Research Letters*, *40*, 429–433. https://doi.org/10.1029/2012GL054329

Mikesell, D., van Wijk, K., Calvert, A., & Haney, M. (2009). The virtual refraction: Useful spurious energy in seismic interferometry. *Geophysics*, *74*(3), A13–A17. https://doi.org/10.1190/1.3095659

Muñoz Sabater, J. (2019). ERA5-land hourly data from 1950 to present. *Copernicus Climate Change Service (C3S) Climate Data Store (CDS)*. https://doi.org/10.24381/cds.e2161bac

Ortiz, H. D., Matoza, R. S., & Tanimoto, T. (2022). Autocorrelation infrasound interferometry on Mars. *Geophysical Research Letters*, *49*(8), e2021GL096225. https://doi.org/10.1029/2021gl096225

Pandey, A., Tkalčić, H., & Ma, X. (2025). Investigating the characteristics of microseisms using the Australian seismic arrays. *Journal of Geophysical Research*, *130*(6), e2024JB031032. https://doi.org/10.1029/2024jb031032

Posmentier, E. S. (1967). A theory of microbaroms. *Geophysical Journal International*, *13*(5), 487–501. https://doi.org/10.1111/j.1365-246x.1967.tb02301.x

Ruigrok, E., Gibbons, S., & Wapenaar, K. (2017). Cross-correlation beamforming. *Journal of Seismology*, *21*(3), 495–508. https://doi.org/10.1007/s10950-016-9612-6

Ruigrok, E., Mikesell, T. D., & van Wijk, K. (2012). Scanning for velocity anomalies in the crust and mantle with diffractions from the core-mantle boundary. *Geophysical Research Letters*, *39*(11), L11301. https://doi.org/10.1029/2012gl051443

Smets, P. S. M., & Evers, L. G. (2014). The life cycle of a sudden stratospheric warming from infrasonic ambient noise observations. *Journal of Geophysical Research*, *119*(21), 12084–12099. https://doi.org/10.1002/2014jd021905

Smink, M. M. E., Assink, J. D., Bosveld, F. C., Smets, P. S. M., & Evers, L. G. (2019). A three-dimensional array for the study of infrasound propagation through the atmospheric boundary layer. *Journal of Geophysical Research*, *124*(16), 9299–9313. https://doi.org/10.1029/2019jd030386

Wapenaar, K. (2006). Nonreciprocal Green's function retrieval by cross correlation. *Journal of the Acoustical Society of America*, *120*(1), EL7–EL13. https://doi.org/10.1121/1.2208153

Waxler, R., & Gilbert, K. E. (2006). The radiation of atmospheric microbaroms by ocean waves. *Journal of the Acoustical Society of America*, *119*(5), 2651–2664. https://doi.org/10.1121/1.2191607

Wessel, P., Smith, W. H. F., Scharroo, R., Luis, J., & Wobbe, F. (2013). Generic mapping tools: Improved version released. *Eos, Transactions American Geophysical Union*, *94*(45), 409–410. https://doi.org/10.1002/2013eo450001

Woolfe, K. F., Lani, S., Sabra, K. G., & Kuperman, W. A. (2015). Monitoring deep-ocean temperatures using acoustic ambient noise. *Geophysical Research Letters*, *42*(8), 2878–2884. https://doi.org/10.1002/2015gl063438